We are IntechOpen, the world's leading publisher of Open Access books
Built by scientists, for scientists

6,900
Open access books available

185,000
International authors and editors

200M
Downloads

Our authors are among the

154
Countries delivered to

TOP 1%
most cited scientists

12.2%
Contributors from top 500 universities

WEB OF SCIENCE™

Selection of our books indexed in the Book Citation Index in Web of Science™ Core Collection (BKCI)

Interested in publishing with us?
Contact book.department@intechopen.com

Numbers displayed above are based on latest data collected.
For more information visit www.intechopen.com

Chapter 3

Studies of Electroconductive Magnetorheological Elastomers

Eugen Mircea Anitas, Liviu Chirigiu and Ioan Bica

Additional information is available at the end of the chapter

http://dx.doi.org/10.5772/intechopen.72732

Abstract

Electroconductive magnetorheological elastomers (MREs) have attracted a wide scientific attention in recent years due to their potential applications as electric current elements, in seismic protection, in production of rehabilitation devices, and sensors or transducers of magnetic fields/mechanical tensions. A particular interest concerns their behavior under the influence of external magnetic and electric fields, since various physical properties (e.g., rheological, elastic, electrical) can be continuously and/or reversibly modified. In this chapter, we describe fabrication methods and structural properties from small-angle neutron scattering (SANS) of various isotropic and anisotropic MRE and hybrid MRE. We present and discuss the physical mechanisms leading to the main features of interest for various medical and technical applications, such as electrical (complex dielectric permittivity, electrical conductivity) and rheological (viscosity) properties.

Keywords: electric field, active magnetic materials, magnetorheological elastomers, magnetodielectric effect, dielectric permittivity, dielectric polarization time

1. Introduction

Magnetorheological materials is a class of smart materials whose electrical, magnetic, mechanical, or rheological properties can be controlled under the application of an external magnetic field. Since their inception [1], magnetorheological materials have evolved into several main subclasses: magnetorheological fluids (MRFs), elastomers (MREs), and gels (MRGs). Generally, they consist of a non-magnetizable phase in which a second phase is embedded. The non-magnetizable phase is usually an elastic matrix based on natural or silicone rubber, while the second one consists of magnetizable nano/microparticles. For MRFs, the non-magnetizable phase is liquid [2, 3], while for MREs it is solid [4]. Although MRFs are the most common magnetorheological materials, their physical properties change with time due to the sedimentation

IntechOpen

© 2018 The Author(s). Licensee IntechOpen. This chapter is distributed under the terms of the Creative Commons Attribution License (http://creativecommons.org/licenses/by/3.0), which permits unrestricted use, distribution, and reproduction in any medium, provided the original work is properly cited. CC BY

process of the magnetizable phase. However, for both conventional [5] and hybrid [6] MREs, this phenomenon does not occur since magnetizable particles are linked to the polymer chains and are fixed in the elastic matrix after curing. In addition, MRFs are known to be a source of environmental contamination and they exhibit sealing problems when used in production of brakes, clutches, or variable-friction dampers [7, 8].

Due to this property, MREs have shown many promising technical, industrial, and bio-medical applications, such as in producing of adaptive tuned vibration absorbers [9], in fabrication of devices for varying the stiffness of suspension bushings [10], electric current elements [11, 12], or seismic protection [13]. Furthermore, MREs can be manufactured in the presence or in the absence of an external magnetic field, depending on the required applications. Usually, this is done at a constant temperature (>120°C) so that the flexibility of the magnetic particles is maintained [14]. In the first case, an isotropic MRE is produced, while in the second one, an anisotropic MRE is obtained [15]. The curing process for anisotropic MREs requires a magnetic field above 0.8 T to align the chains [14]. At the end of curing process, the magnetic particles are fixed inside the elastic matrix. By formation of parallel chains of magnetizable nano/microparticles along the magnetic field lines, drastic changes of the elasticity coefficients [16] and of the main shear tensions [17] can be induced in MREs. Therefore, knowledge of the nano/microstructure has fundamental implications in the production of various types of novel MREs with predetermined properties and functions.

The structural analysis of MREs is performed mainly by using electron microscopy, computed tomography (CT) or small-angle scattering [18, 24] (SAS; neutrons or X-rays) techniques. Real-space analysis (i.e., electron microscopy or CT) is in principle more powerful than reciprocal-space analysis (i.e., SAS), but usually it requires extensive sample preparation, and as a consequence the same sample cannot subsequently be used for additional investigations. These disadvantages can be overcome by CT, which gives a three-dimensional (3D) representation of the structure, but it is difficult to resolve structures smaller than few micrometers. A solution to this issue is provided by small-angle scattering techniques [19, 37, 38]. Although the loss of information in scattering is a severe limitation, SAS technique has the advantage that it is suitable for structures with dimensions within 1–1000 nm and the quantities of interest are averaged over a macroscopic volume. In particular, small-angle neutron scattering (SANS) is very useful in studying magnetic properties of materials or in emphasizing certain features [20–25] since neutrons interact with the atomic nuclei and with the magnetic moments in the sample.

In particular, for MREs in which the matrix and/or the fillers form self-similar structures (either exact or statistical) [26, 27], the most important advantage is that scattering methods can distinguish between mass [28] and surface fractals [29]. From an experimental point of view, the difference is accounted through the value of the scattering exponent τ in the region where the SAS intensity $I(q)$ has a power-law decay, that is,

$$I(q) \propto q^{-\tau}, \tag{1}$$

where $q = (4\pi/\lambda)\sin\theta$ is the scattering vector, λ is the wavelength of the incident radiation, and 2θ is the scattering angle. In terms of the fractal dimensions, the scattering exponent in Eq. (1) can be written as

$$\tau = \begin{cases} D_{\mathrm{m}}, & \text{for mass fractals} \\ 6 - D_{\mathrm{s}}, & \text{for surface fractals} \end{cases}, \tag{2}$$

where D_{m} is the mass fractal dimension with $0 < D_{\mathrm{m}} < 3$, and D_{s} is the surface fractal dimension with $2 < D_{\mathrm{s}} < 3$. Thus, when the measured absolute value of the scattering exponent is smaller than 3, the sample is considered to be a mass fractal with fractal dimension τ, while if the exponent is between 3 and 4, the sample is considered to be a surface fractal with fractal dimension $6 - \tau$. The mass fractal dimension describes the way in which the mass $M(r)$ of a disk centered on the fractal varies with its radius r. The closer the value is to 3, the more compact is the structure. The surface fractal dimension describes the way in which the surface varies with the radius. When its value is close to 3, the fractal is so folded that it fills the space almost completely. However, when its value is close to 2, the surface is almost smooth. Therefore, for a mass fractal $D_{\mathrm{s}} = D_{\mathrm{m}} < 3$, while for a surface fractal, we have $D_{\mathrm{m}} = 3$ [30, 31].

For MREs, both the compactness of the structures formed as well as their roughness is mainly influenced by the volume fraction of the magnetizable phase or additives consisting of electroconductive particles, and by the internal structure of the matrix. In turn, by varying these parameters, various physical characteristics, such as dispersion and absorption characteristics of an electromagnetic field, or the electrical conductivity [32] can be tuned in the presence of an electric field superimposed over a magnetic one. Practically, a common way to perform such tuning is by preparing membranes based on MREs and placing them between two electrodes. In this way, they will act either as electric capacitors or as magnetoresistors whose output signals can be modified in the presence of an electric and/or magnetic field [33–35].

In this chapter, we present the fabrication process of few types of magnetorheological and magnetic elastomers based on silicone rubber (SR), silicone oil (SO), turmeric, carbonyl iron (CI), cotton fabric, Stomaflex, and Nivea creme. By using MREs, we fabricate membranes which are introduced between two plates and thus forming electrical capacitors. The structural properties are determined both in real and reciprocal space, by using scanning electron microscopy (SEM) and SANS. For the MREs, we investigate the behavior of the equivalent electrical capacitance C_p, and respectively of the equivalent resistance R_p in a magnetic field with or without an electric field. The effect of volume concentration of various microparticles on the components of complex relative permittivity, electrical conductivity, and on viscosity is investigated by using the dipolar approximation. The components of elasticity, of mechanical tensions, and the modulus of elasticity are presented in the framework of a model based on elasticity theory.

2. Preparation of electroconductive magnetorheological elastomers

In this section, we present the materials and the fabrication methods used for preparation of several new classes of elastomers nanocomposites. For this purpose, we use materials with possible applications in biomedicine, consumer goods, and rubber engineering. The internal structure of elastomers is revealed with the help of SEM images.

2.1. Magnetic elastomers based on Stomaflex Creme and silicone oil

In this example, the base matrix is a complex medium in which the magnetic phase is dispersed and consists of a condensation curing a polysiloxane impression material, which is conventionally used in dental medicine. It is a low-viscosity, light-bodied, syringeable, and reline material for functional impressions, commonly known as Stomaflex Creme. The chemical components are polydimethylsiloxane, calcium carbonate, taste ingredients, and catalyst (dibutyitindilaureate, benzyl silicate and pigments). The base matrix is then mixed with silicone oil, and **Figure 1** (left part), presents an SEM of the final polymer matrix. The image shows that the matrix has a rough surface. Quantitatively, this is characterized by a surface fractal dimension of about $D_s = 2.47$ [23]. Generally, the surface fractal dimension lies between 2 and 3. A value close to 2 indicates a surface almost completely planar, while a value close to 3 indicate a surface so folded that it almost fills all the available space.

The magnetic phase consists of Fe particles with a mean radius of about 2 μm. **Figure 1** (right part) presents an SEM of the polymer matrix together with the magnetizable particles. From a structural point of view, the presence of the magnetizable particles alters the roughness of the matrix and thus the value of the surface fractal dimension is changed [23].

Depending on the required applications, the magnetic elastomer can be polymerized with or without magnetic field at various concentrations of Fe microparticles [23]. Furthermore, additives can also be used to keep magnetizable particles apart from each other. However, this issue arises mainly in MRFs, where additives have to hinder the sedimentation process.

2.2. Magnetic elastomers based on silicone rubber and magnetic liquid

For this class of magnetic elastomers, the matrix is a silicone rubber (SR) reinforced with silicone oil (SO), stearic acid (SA), catalyst (C), and magnetic liquid (ML) at various concentrations. ML contains magnetizable nanoparticles, oleic acid, and crude oil, and it has a density of 1.465 g/cm^3. Initially, an SA solution is prepared, which is then heated for homogeneity up to 350 K. This solution has the property that at about 300 K, it is in liquid phase, while at lower temperatures it crystallizes. Then, a homogeneous mixture is prepared by using SR, SA solution, C, and ML at

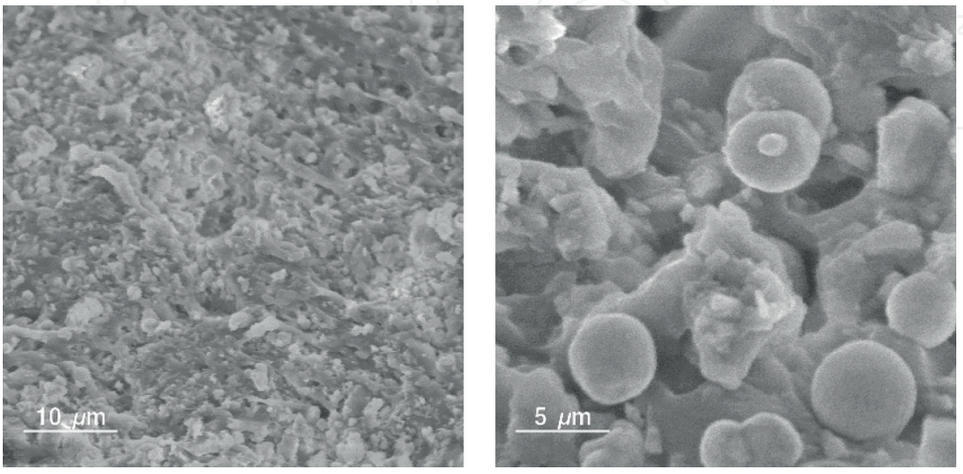

Figure 1. SEM images from MREs based on Stomaflex Creme and Fe microparticles [23]. Left part: The polymer matrix. Right part: The polymer matrix together with magnetizable phase.

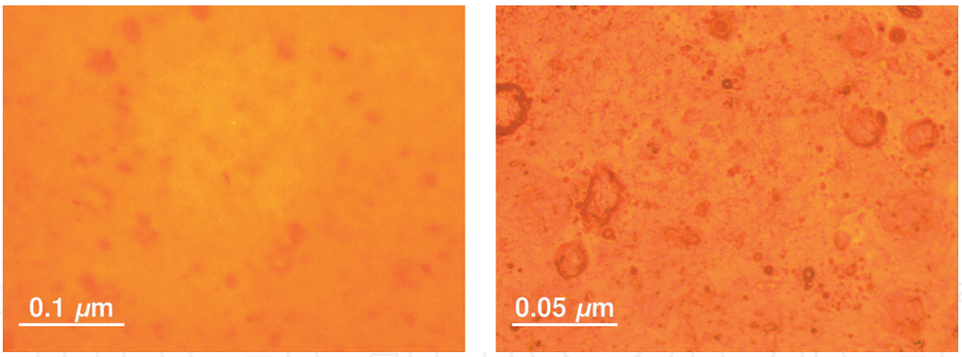

Figure 2. Electron microscopy images from magnetic elastomers based on silicone rubber and reinforced with silicone rubber, silicone oil, catalyst and magnetic liquid [27]. Left part: 1%vol. conc. Right part: 2%vol. conc.

various concentrations. Further, each new mixture is poured between two polyethylene thin foils and pressed in-between two parallel plates. After polymerization of about 24 h, we obtain the elastomeric magnetic membranes [27]. **Figure 2** (Left and Right) parts show the electron microscopy images for 1%vol. conc. and 2%vol. conc. of ML, respectively.

2.3. Magnetorheological elastomers based on silicone oil and Fe nano-/microparticles

An important class of MREs is based on silicone oil and reinforced with Fe nano/micro particles, since this gives electrical properties of importance for various particular applications. The materials used for producing this class of MRE are SO (with viscosity 200 mPa s at 260 K), Fe content of min. 97% and mass density 7860 kg/m^3, CI spherical micro particles with diameters between 4.5 and 5.4 μm, graphene nanoparticles (nGr) with granulation between 6 and 8 nm, cotton fabric gauze bandage (GB) (**Figure 3**, left part), and copper-plated textolite (*TCu*).

Based on these materials we prepare membranes (**Figure 3**, right part), following similar procedures as presented first in [6, 36]. First, homogeneous solutions are prepared by keeping constant the volume concentration of SO and CI, and by varying the volume concentration of SR and nGr. Each solution has a volume of 5 cm^3. Pieces of GB and copper-plated textolite are cut in rectangular shapes with sides 5×4 cm, and 5×5 cm respectively. Each GB cotton fabric is

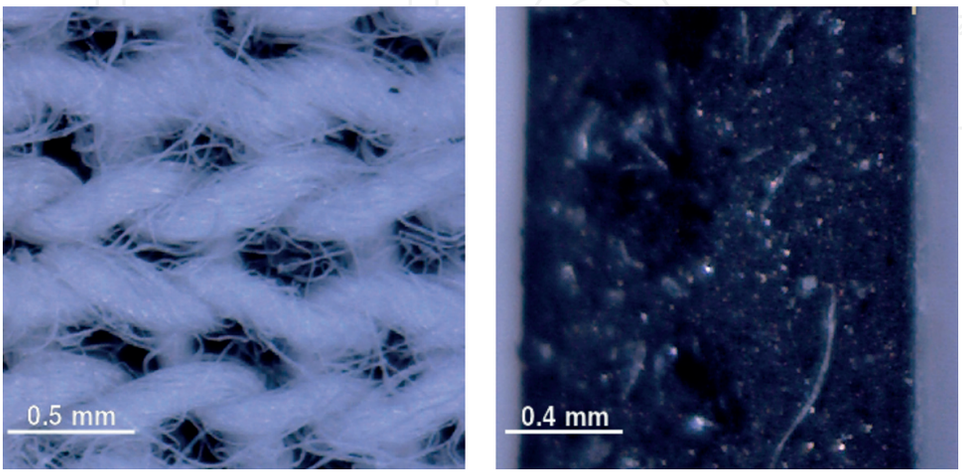

Figure 3. Left part: Electron microscopy of cotton fabric. Right part: Electron microscopy images from magnetic elastomers based on silicone rubber and reinforced with silicone rubber, and graphene nanoparticles [6, 36].

impregnated with solutions, which are then deposited on the copper-side plates of copper-plated textolite. Then, the impregnated cotton fabric is introduced between the copper-side plates in such a way that an edge of 0.5 cm of TCu remains uncovered. Finally, the whole system is compressed.

3. Structural properties using SANS

3.1. Theoretical background

In a SANS experiment, a beam of neutrons is emitted from a source and is directed toward the sample. In a scattering process, a small fraction is deviated from its initial path and is recorded by the detector. By considering that the scattering objects have the length b_j, then the scattering length density SLD can be written as $\rho(\boldsymbol{r}) = \sum_j b_j(\boldsymbol{r} - \boldsymbol{r}_j)$ [38], where $\boldsymbol{r}_j$ are the positions vectors. In a particulate system where the particles have density ρ_m and the matrix has density ρ_p, the excess scattering SLD is d $\Delta\rho = \rho_m - \rho_p$. We consider also that the objects are randomly distributed and their positions are uncorrelated. Thus, the scattering intensities can be written as [37, 38] $I(q) = n|\Delta\rho|^2 V^2 \left\langle |F(\boldsymbol{q})|^2 \right\rangle$, where n is the concentration of objects, V is the volume of each object, and $F(\boldsymbol{q}) = 1/V \int_V e^{-i\boldsymbol{q}\cdot\boldsymbol{r}} \mathrm{d}^3 r$.

Many experimental SANS curves are characterized by a simple power-law of the type

$$I(q) = Aq^{-\tau} + B, \tag{3}$$

where B is the background. Depending on the value of scattering exponent τ, reflects the dimensionality of the object. **Figure 4** (left part), shows the corresponding simple power-law decay at fixed values of A and B, for $\tau = 1$ (this rods), $\tau = 2$ (thin disks), $\tau = 2.5$ and 3.5 for fractals, and $\tau = 4$ (3D objects).

However, a large number of SANS data obtained from MRE shows a succession of two power-law decays with arbitrarily exponents on a double logarithmic scale. This indicates the formation of a complex structure with two hierarchical levels. Therefore, for these data the Beaucage

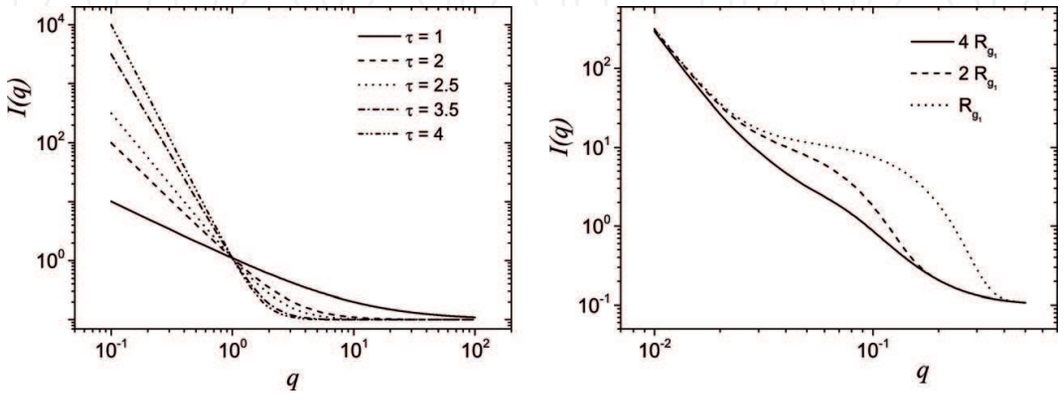

Figure 4. Left part: Simple power-law decays given by Eq. (3) for various values of the scattering exponent τ. Continuous curves – Scattering from regular objects. Dashed curves – Scattering from fractal objects. Right part: Scattering intensity given by Beaucage model in Eq. (4) for various values of the radius of gyration of the smallest hierarchical level.

model [39] is most commonly used. However, under some conditions a SANS experiment can show only a single power-law decay, and therefore only a single structural level can be investigated. For a two-level structure, the intensity can be approximated by [39]:

$$I(q) \propto G_1 e^{\frac{-q^2R_{g1}^2}{3}} + B_1 e^{\frac{-q^2R_{g2}^2}{3}} \left(\frac{h_1}{q}\right)^{D_1} + G_2 e^{\frac{-q^2R_{g2}^2}{3}} + B_2 \left(\frac{h_2}{q}\right)^{D_2} + B. \quad (4)$$

Here, $h_1 = \mathrm{erf}\left(qR_{g1}/\sqrt{6}\right)^3/q$, $h_2 = \mathrm{erf}\left(qR_{g2}/\sqrt{6}\right)^3/q$ and B is the background. The first term in Eq. 4 describes a large-scale structure of overall size R_{g1} composed of small-scale structures of overall size R_{g2}, written in the third term. The second term allows for mass or surface fractal power-law regimes for the large structure. G_1 and G_2 are the classic Guinier prefactors, and B_1 and B_2 are the prefactors specific to the type of power-law scattering, specified in the regime in which the exponents D_1 and D_2 fall. **Figure 4** (right part) shows the scattering given by Beaucage models when the radius of gyration of the smaller structural level is varied, while all the other parameters are kept constant. For small values of the radius of gyration, the curves clearly show the appearance of a plateau (at about $4 \times 10^{-2} \lesssim q \lesssim 10^{-1}$), which may indicate that the sizes of the scattering units are much smaller than the distances between them. Similar behavior of the scattering curve has been observed also in [40–48].

3.2. SANS from magnetic elastomers based on Stomaflex Creme and silicone oil

Figure 5 shows the SANS curves on a double logarithmic scale, corresponding to a polymer matrix consisting of Stomaflex creme and silicone oil (Left part), as well as the polymer matrix in which were embedded Fe particles (Right part) (see Ref. [24]). For the case of scattering from the polymer matrix, the experimental data are characterized by the presence of two successive simple power-law regions, with different values of the scattering exponents. Thus, these data can be modeled by using the simple power-law given by Eq. (3). At low values of the scattering wavevector $q\left(8 \times 10^{-3} \lesssim q\ \left(\text{Å}^{-1}\right) \lesssim 2.2 \times 10^{-2}\right)$, the absolute value of the scattering exponent is 3.88. This indicates that in this range the scattering signal arises from a surface fractal with fractal dimension $D_1 = 6 - 3.88 = 2.12$, which represents a very smooth surface. However, at higher values of the scattering wavevector ($2.2 \times 10^{-2} \lesssim q\ \left(\text{Å}^{-1}\right) \lesssim 2 \times 10^{-1}$), the absolute value of the

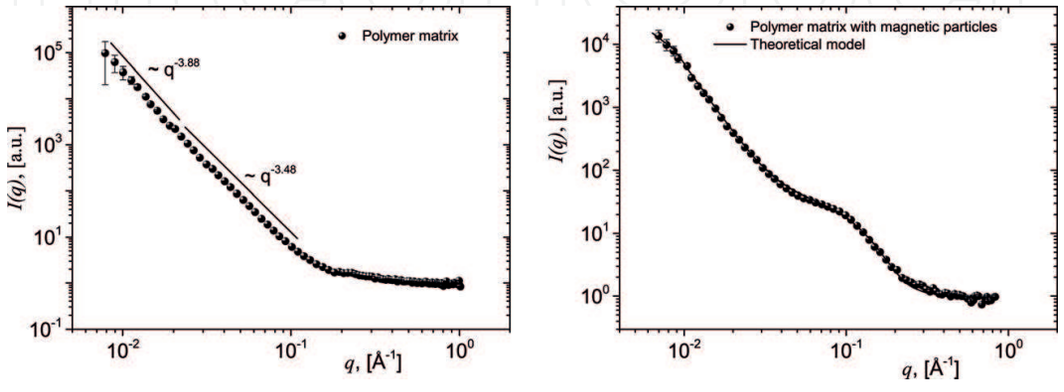

Figure 5. Left part: Scattering from the polymer matrix based on Stomaflex creme and silicone oil. Right part: Scattering from the polymer matrix with magnetic Fe particles.

scattering exponent decreases to 3.48, which indicates the presence of a more rough surface, with the fractal dimension $D_2 = 6 - 3.48 = 2.52$.

When magnetic particles are added, the SANS curve shows the presence of two simple power-law decays but with an additional "knee" in-between them, which arise at $q \simeq 1.5 \times 10^{-1}\left(\text{Å}^{-1}\right)$ (**Figure 5**, right part). This shows the formation of multilevel structures in the magnetic elastomers and the Beaucage model (Eq. (4)) is generally used to extract information about the fractal dimensions and the overall size of each structural level. For the data shown in **Figure 7**, a fit with the Beaucage model reveals that the fractal dimensions of the two structural levels are $D_1 = 2.7$ and $D_2 = 2.4$, while the overall sizes are $R_{g_1} \geq 79$ nm and $R_{g_2} = 4.5$ nm, respectively.

3.3. SANS from magnetic elastomers based on silicone rubber and magnetic liquid

The SANS data from a polymer matrix based on silicone rubber (sample M_1) reinforced with magnetic particles at various concentrations are shown in **Figure 6** (left part) (see Ref. [27]). As in the previous case, the scattering data from the polymer matrix show a single power-law decay with the fractal dimension $D_1 = 2.62$. This shows the formation of a mass fractal with very ramified branches. Addition of magnetic particles leads to a two-level structure. For the sample with the lower concentration of particles (sample M_2), the Beaucage model gives $D_1 = 2.68$, $D_2 = 3.21$, $R_{g_1} = 34$ nm, and $R_{g_2} = 3$ nm. For the sample with the higher concentration of magnetic particles (sample M_3), one obtains $D_1 = 2.68$, $D_2 = 3.21$, $R_{g_1} = 34$ nm, and $R_{g_2} = 3$ nm. This complex arrangement shows that a mass fractal of nearly constant fractal dimension is composed of surface fractals whose fractal dimension increases significantly with increasing concentration of magnetic phase.

Another useful visual representation is by plotting the data after subtracting the contribution of the polymer matrix. This leads to the appearance of pronounced peaks, from which an estimation of the overall sizes can be inferred (**Figure 6**).

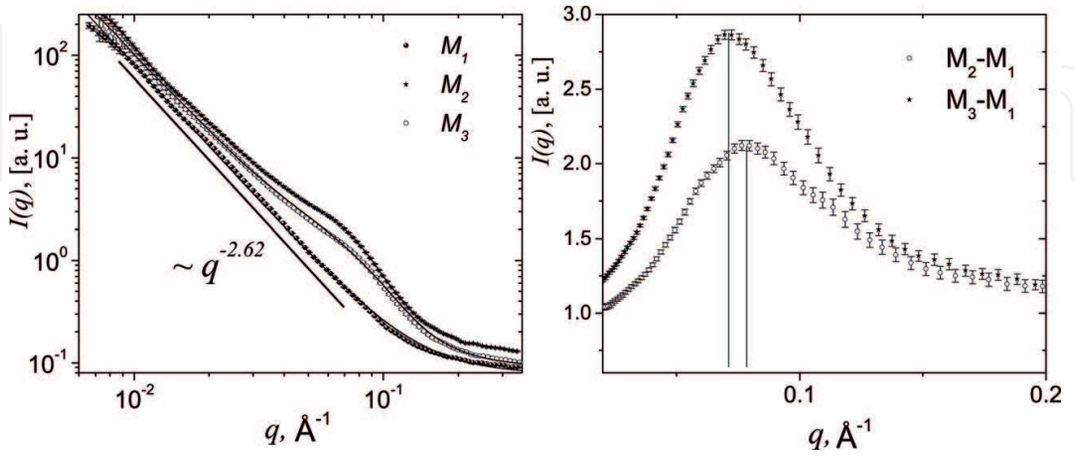

Figure 6. Left part: Scattering from polymer matrix based on silicone rubber (sample M_1) and scattering from polymer matrix with various concentrations of magnetic particles (samples M_2 and M_3). Right part: Contribution only of the particles. The vertical lines indicate the maximum size of the second structural level.

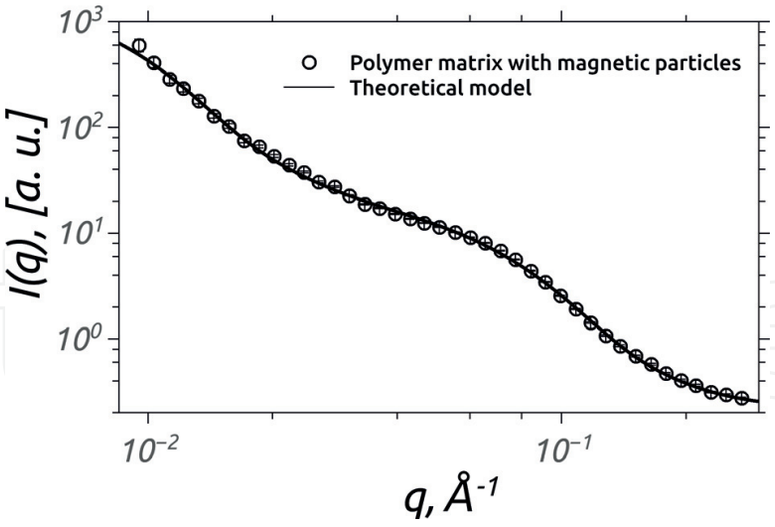

Figure 7. Scattering from the polymer matrix based on silicone rubber with graphene nanoparticles.

3.4. SANS from magnetorheological elastomers based on silicone oil and *Fe* nano-/microparticles

Another example of materials displaying a complex hierarchical organization in which fractal structures are formed, is presented for magnetorheological elastomers based on silicone rubber and graphene nanoparticles. Since, as expected, the SANS data of the matrix reinforced with graphene particles show a "knee" (**Figure 7**), the main structural characteristics are obtained using Eq. (4). Fitting the data reveals a complex fractal structure of size $R_{g1} \simeq 290$ Å, which consists of smaller structures of size $R_{g2} \simeq 35$ Å. The corresponding fractal dimensions are $D_1 = 2.51$ and $D_2 = 2.38$. This reveals the formation of fractal structures consisting of structural units, which are also fractals.

4. Physical properties of MRE-based membranes

The values of the corresponding fractal dimensions in such systems may help to understand the aggregation process and the interaction processes between particles, on the one hand, and between the polymer matrix, on the other hand. In turn, this may provide a better understanding of the physical properties, of various types of materials, such as membranes, based on these components. As an application, we shall present below in more detail the experimental setup and the fabrication process of a class of MRE-based membranes and study the electrical and rheological properties in the presence of a magnetic field.

4.1. Experimental setup and fabrication method

The materials used for manufacturing MRE-based membranes doped with graphene nanoparticles (nGr) are: silicone oil (SO), AP200 type, with viscosity 200 m Pa s at temperature 260 K; carbonyl iron (CI) spherical particles, *C*3518 type with diameters between 4.5 and 5.4 μm, Fe content of min. 97% and mass density 7860 kg/m^3; nGr with granulation between

6 and 8 nm; cotton fabric gauze bandage (GB), with the texture shown in **Figure 3** (left part); silicone rubber (SR) (black color); copper-plated textolite (TCu) with a thickness of 35 μm.

The MRE-based membranes are fabricated by performing the following steps: first, three homogeneous solutions are prepared with the chemical composition shown in **Table 1**. Each solution has a volume of 5 cm^3; three pieces of GB are cut in rectangular shapes with sides 5×4 cm, and six plates of TCu are cut also in rectangular shapes, with dimensions 5×5 cm; each GB cotton fabric is impregnated with solutions S_i, $i = 1, 2, 3$. Solutions are also deposited on the copper-side plates of TCu; the impregnated cotton fabric is introduced between the copper-side plates such that an edge of 0.5 cm of TCu is not covered, and then the whole system is compressed.

Using these solutions, we build a plane electrical capacitor FC_1 that corresponds to S_1, a second capacitor FC_2 that corresponds to S_2, and a third capacitor that corresponds to FC_3. We use GB for strengthening the membranes. The polymerization time is approximately 24 h. At the end of the polymerization process, one obtains three capacitors having as dielectric materials the membranes *Ms* with sizes 5×4 cm whose composition and thickness d_0 are listed in **Table 2**.

Figure 3 shows the experimental configuration used for studying the MRE-based membranes in magnetic field. It consists of an electromagnet with a coil and a magnetic core current source, an RLC-meter, and a current source. The electric capacitor is placed between the poles of the electromagnet. The magnetic field intensity is measured with a gaussmeter. Magnetic field intensity can be continuously modified, through the intensity of the electric current provided by the source (A).

By changing the frequency f of the electric current, we measure the equivalent capacitance (C_p) and resistance (R_p) of *FC*. We determine that for $f = 10$ kHz, the measured values are stable in time. Then we fix the frequency f at this value and we vary the magnetic field intensity H from 0 to 200 kA/m.

4.2. Electrical and rheological properties

Figure 8 shows that the capacitance increases while the resistance decreases with increasing magnetic field intensity. The volume fraction Φ of nGr greatly influences the values of the equivalent capacitance and of resistance, respectively, for fixed values of magnetic field intensity.

In the presence of a magnetic field, the carbonyl iron microparticles become magnetized, and form magnetic dipoles which attract each other along the direction of H. The equation of motion is [49]

S_i	**SR** (cm^3)	**SO** (cm^3)	**CI** (cm^3)	**nGr** (cm^3)
S_1	3.0	1.0	1.0	0.0
S_2	2.6	1.0	1.0	0.4
S_3	2.0	1.0	1.0	1.0

Table 1. Chemical compositions and the volumes (in cm^3) for each component $S_i, i = 1, 2, 3$.

Ms	SR (vol.%)	SO (vol.%)	CI (vol.%)	nGr (vol.%)	d_0 (mm)
M_1	60	20	20	0	4.30
M_2	52	20	20	8	3.90
M_3	40	20	20	20	4.46

Table 2. Chemical compositions and volume concentrations (%vol.) for membranes $M_i, i = 1, 2, 3$.

$$M\ddot{\chi} + 2\beta\dot{\chi} + \frac{3\mu_0}{\pi}\frac{\mu_s}{x^4}m^2 = 0, \tag{5}$$

where M is the mass of the magnetic dipole, 2β is the particle friction coefficient, x is the distance between two neighboring dipoles, m is the magnetic dipole moment, μ_0 and μ_s are the magnetic permeability of vacuum, and of SR, respectively. At $t = 0$, when the magnetic field is applied, the distance between the magnetic dipoles is [50] $X_0 = d_m/\sqrt[3]{\phi}$, where ϕ is the volume fraction of magnetic dipoles, and which coincides with the volume fraction of CI. For membranes with CI and nGr, the distance between the magnetic dipoles at $t = 0$ can be calculated using [50] $X_0^{nGr} = d_m/\sqrt[3]{\phi(1+\Phi)}$. Here, Φ is the volume fraction of nGr.

For membranes without nGr, the following conditions shall be satisfied:

$$x = \begin{cases} X_0, & \text{at } t = 0 \text{ and } H \neq 0, \\ x, & \text{at } t \neq 0 \text{ and } H \neq 0, \end{cases} \tag{6}$$

while for membranes with *nGr*, we have the conditions

$$x = \begin{cases} X_0^{nGr}, & \text{at } t = 0 \text{ and } H \neq 0, \\ x_{nGr}, & \text{at } t \neq 0 \text{ and } H \neq 0. \end{cases} \tag{7}$$

By using numerical values $d_m = 5\ \mu m$ for the mean diameter of CI particles, and $\rho_m = 7860\ \text{kg/m}^3$, the mass of magnetic dipole becomes $M \equiv \pi\rho_m d_m^3/6 = 0.514 \times 10^{-12}$ kg. Further, the quantity 2β in Eq. (5) can be approximated by $2\beta = 3\pi\eta d_m$, where η is the viscosity. Thus, for $0.1 \leq \eta(Pa\ s) \leq 100$, we obtain the variation of the particle friction coefficient: $47.1 \times 10^{-7} \leq 2\beta(N) \leq 47.1 \times 0^{-4}$. Knowing that [49] $m = \pi d_m^3 \chi H/6$, where $\chi = 3\left(\mu_p - \mu_s\right)/\left(\mu_p + \mu_s\right)$ and

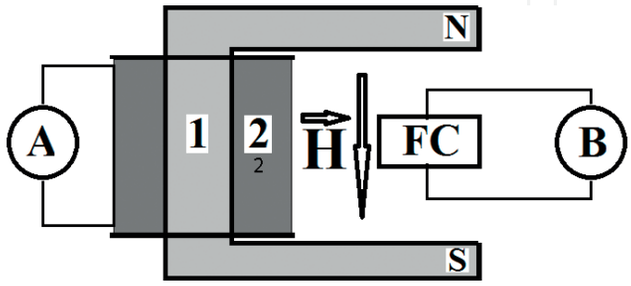

Figure 8. Experimental setup (overall configuration): *FC*–plane capacitor, *H*–magnetic field intensity, 1–magnetic core, 2–coil, A–source of continuous current, B–*RLC*–meter, *N* and *S*–magnetic poles [6].

since $\mu_p \gg \mu_s$, we can write in a good approximation that $\chi = 3$, where μ_p is the magnetic permeability of CI microparticles.

Since $8 \le H(kA/m) \le 200$, then $1.57 \times 10^{-8} \le m\left(A\,cm^2\right) \le 3.92 \times 10^{-7}$. Further, by using $d_m = 5\,\mu m$ and $\phi = 20\%$, we obtain the distance between magnetic dipoles $X_0 = 8.55\,\mu m$. Taking into account that $\mu_s = 1$ and $\mu_0 = 4\pi 10^{-7}$H/m, we obtain $0.55 \times 10^{-9} \le 3\mu_0\mu_s m^2/\left(\pi x^4\right)\,(N) \le 0.345 \times 10^{-6}$. Therefore, Eq. (5) becomes

$$2\beta\dot{x} + \frac{3\mu_0}{\pi}\frac{\mu_s}{x^4}m^2 = 0. \tag{8}$$

Using the numerical values $\chi = 3$ and $x = d_m$ into Eq. (8), we can write the equation of motion of magnetic dipoles along the magnetic field, such as

$$2\beta\dot{x} + \frac{3\pi\mu_0}{4}\mu_s d_m^2 H^2 = 0. \tag{9}$$

By integrating the last equation, and using the initial and boundary conditions, we obtain

$$x = X_0 - \frac{3\pi\mu_0}{8\beta}\mu_s d_m^2 H^2 t. \tag{10}$$

Then, from Eq. (10), the distance between two magnetic dipoles can be written as

$$x = d_m 1\sqrt[3]{\frac{}{\phi}}\left(1 - 3\pi\sqrt[3]{\phi}\frac{\mu_0}{8\beta}\mu_s d_m^2 H^2 t\right). \tag{11}$$

Following a similar procedure for the membrane with nGr, the equation of motion of magnetic dipoles becomes

$$x_{nGr} = d_m 1\sqrt[3]{\frac{}{\phi(1+\Phi)}}\left(1 - 3\pi\sqrt[3]{\phi(1+\Phi)}\frac{\mu_0}{8\beta}\mu_s d_m^2 H^2 t\right). \tag{12}$$

The number of magnetic dipoles from the membrane can be calculated according to [36] $N \equiv V\phi V_d = 6Lld_0/\left(\pi\phi(1+\Phi)d_m^3\right)$, where V is the membrane's volume, V_d is the average volume of *CI* microparticles, and L, l, and d_0 are the length, width, and the thickness of the membrane, respectively. The maximum number of dipoles from each chain is $N_1 = d_0 d_m$, and the total number of dipoles is $N_2 \equiv N/N_1 = 6Ll/\left(\pi\phi(1+\Phi)d_m^2\right)$. In a magnetic field, the membrane's thickness can be approximated by the relation $d = (N-1)x$, which together with Eq. (12) gives (for $N_1 \gg 1$):

$$d = d_0 1\sqrt[3]{\frac{}{\phi(1+\Phi)}}\left(1 - 3\pi\sqrt[3]{\phi(1+\Phi)}\frac{\mu_0}{8\beta}\mu_s d_m^2 H^2 t\right). \tag{13}$$

On the other hand, the electrical capacitance of the capacitor can be calculated from $C_p = \varepsilon_0\varepsilon_r' Ll/d$, where ε_0 is the absolute permittivity of vacuum, ε_r' is the real component of the

complex relative permittivity and d is the thickness of the membrane for plane capacitors in magnetic field.

The equivalent resistance of FC is modeled by the resistance of a linear resistor, namely, $R_p = d/(\sigma Ll)$, where σ is the electrical conductivity of the membrane, and can be approximated by [51] $\sigma = 2\pi f \varepsilon_0 \varepsilon_r''$. Here, f is the frequency of the electric field and ε_r^* is the imaginary part of the complex relative permittivity. Thus, the variation of the equivalent electrical capacitance, with the magnetic field intensity becomes

$$C_p = \frac{C_{p_0}}{1 - 3\pi \sqrt[3]{\phi(1+\Phi)}\,\frac{\mu_0}{8\beta}\mu_s d_m^2 H^2 t,} \tag{14}$$

where, $C_{p_0} = \varepsilon_0 \varepsilon_{r_0}' Ll\sqrt[3]{\phi(1+\Phi)}/d_0$ is the equivalent capacitance of FC at $H = 0$, and ε_{r_0}' is the real component of the complex relative permittivity at $H = 0$. Similarly, the equivalent resistance can be obtained from

$$R_p = R_{p_0}\left(1 - 3\pi \sqrt[3]{\phi(1+\Phi)}\,\frac{\mu_0}{8\beta}\mu_s d_m^2 H^2 t\right), \tag{15}$$

where $R_{p_0} = 1/(\sigma Ll) \times d_0/\sqrt[3]{\phi(1+\Phi)}$ is the equivalent electrical resistance of FC at $H = 0$.

The imaginary part of complex relative permittivity can be obtained using Eq. (13): $\varepsilon_r'' = d/\left(2\pi f R_p Ll\right)$. Eqs. (14) and (15) show that C_p increases and R_p decreases with increasing H^2. Then, the real component of the complex relative permittivity is obtained as:

$$\varepsilon_r' = \frac{C_p d}{\varepsilon_0 Ll}. \tag{16}$$

For $C_p = C_p(H)_\Phi$ shown in **Figure 9** (left part), $d \approx d_0$, $L = 0.05$ m, and respectively for $l = 0.04$ m, we obtain $\varepsilon_r' = \varepsilon_r'(H)_\Phi$, as shown in **Figure 10** (left part). From the dependence $R_p = R_p(H)_\Phi$ shown in **Figure 9** (right part), we obtain the variation $\varepsilon_r'' = \varepsilon_r''(H)_\Phi$ as shown in **Figure 10** (right part).

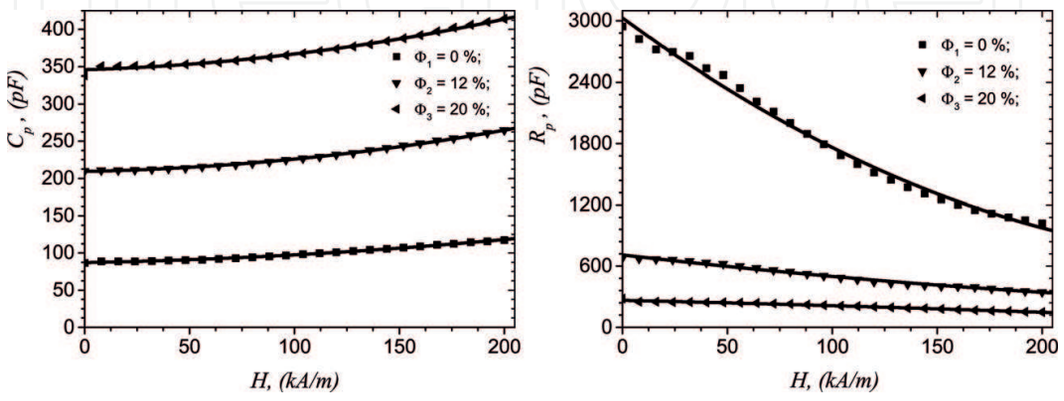

Figure 9. Left part: Capacitance. Right part: Resistance of FC, as a function of magnetic field intensity H. Discrete points – Experimental data, continuous line – Polynomial fit.

From the dependencies $\varepsilon_r'' = \varepsilon_r''\ (H)_\phi$ and $\varepsilon_r' = \varepsilon_r'(H)_\phi$ shown in **Figure 5** we obtain:

$$\varepsilon_r'' = \begin{cases} -11.5 + 0.8\varepsilon_r' - 0.0094\left(\varepsilon_r'\right)^2, & for\ M_1, \\ -52.0 + 1.720\varepsilon_r' - 0.014\left(\varepsilon_r'\right)^2, & for\ M_2, \\ -58.0 + 0.998\varepsilon_r' - 0.015\left(\varepsilon_r'\right)^2, & for\ M_3, \end{cases} \tag{17}$$

The points $\left(\varepsilon_r', \varepsilon_r''\right)$ are found on continuous semicircles (see **Figure 11**; left part) [6], and their values at a fixed H depend on the volume fraction of nGr. For fixed electrical frequency $f = 10$ kHz of the electric field, and for $\varepsilon_r'' = \varepsilon_r''(H)_\Phi$ we obtain the dependency of electrical conductivity $\sigma = \sigma(H)_\Phi$ as shown in **Figure 11** (right part). The results show that the electrical conductivity increases with magnetic field intensity, and the obtained values increase sensibly with increasing the quantity of graphene nanoparticles.

With the help of Eq. (15) we can write that: $2\beta = 3\pi\sqrt[3]{\phi(1+\Phi)}\mu_0\mu_s d_m^2 H^2 t/8\left(1 - R_p/R_{p_0}\right)$, and using the relation $2\beta = 3\pi\eta d_m$, we obtain the viscosity of the membranes:

$$\eta = \sqrt[3]{\phi(1+\Phi)}\frac{\mu_0}{8\left(1 - \frac{R_p}{R_{p0}}\right)}\mu_s d_m^2 H^2 t. \tag{18}$$

Using Φ listed in **Table 2**, together with $\phi = 20\%$, $d_m = 5\ \mu m$, $t = 5$ s, and the functions $R_p/R_{p_0} = R_p/R_{p_0}(H)_\Phi$, into Eq. (18), we obtain:

$$10^7\ \eta_1(\text{Pa s}) = 22.922\ H^2(\text{kA/m})\frac{1}{\left(1 - \frac{R_p}{R_{p0}}\right)_{\Phi_1}}, \tag{19}$$

$$10^7\ \eta_2(\text{Pa s}) = 23.820\ H^2(\text{kA/m})\frac{1}{\left(1 - \frac{R_p}{R_{p0}}\right)_{\Phi_4}}, \tag{20}$$

$$10^7\ \eta_3(\text{Pa s}) = 24.374\ H^2(\text{kA/m})\frac{1}{\left(1 - \frac{R_p}{R_{p0}}\right)_{\Phi_6}}, \tag{21}$$

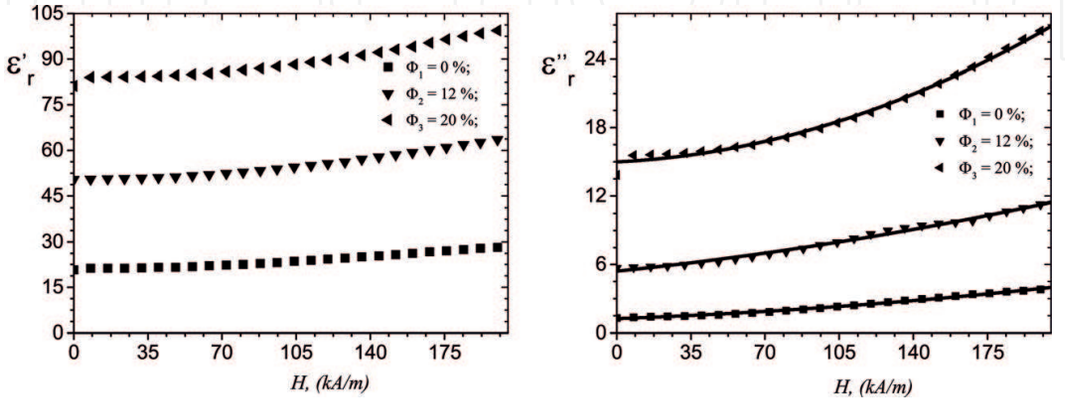

Figure 10. Variation of dielectric permittivity (left part), and of dielectric loss factor (right part), with magnetic field intensity.

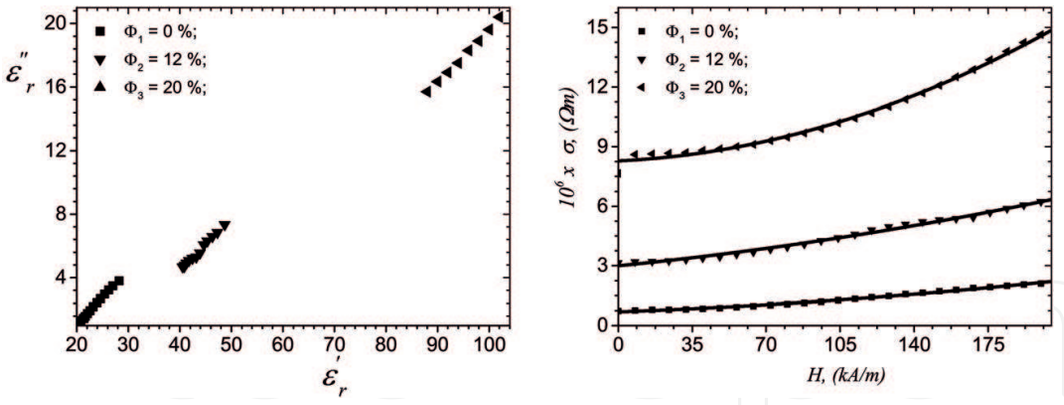

Figure 11. Left part: Cole-Cole diagrams for the membranes *Ms;* right part: Variation of electrical conductivity σ with magnetic field intensity *H*.

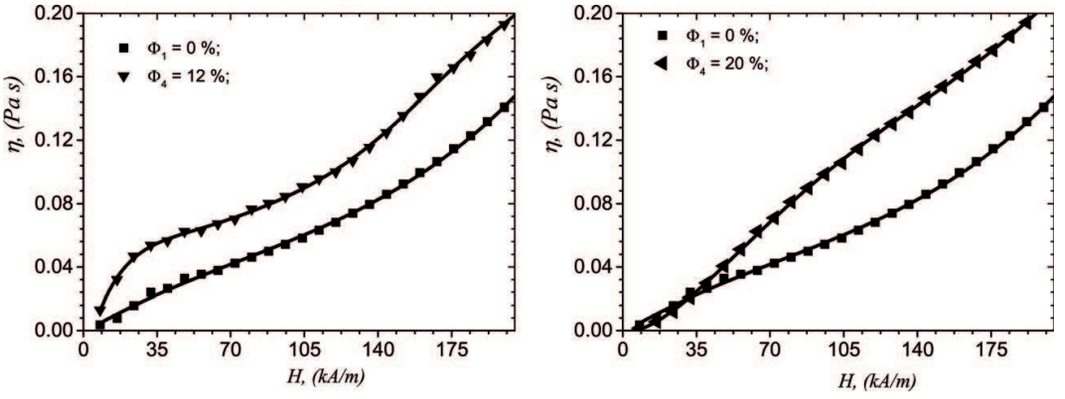

Figure 12. Variation of viscosity with magnetic field. Points – Experimental data, line – Polynomial fit.

This shows that viscosity increases with increasing the magnetic field intensity and is sensibly influenced by the nGr concentration as shown in **Figure 12**. By increasing the volume concentration of nGr, the space between the polymer molecules is saturated with nGr. Depending on the available space provided by the matrix, this increase may lead to formation of complex multilevel structures, in which one fractal (either mass or surface) consists of another fractal, as discussed in Section 3.

5. Conclusions

In this chapter, by using the EM and SANS techniques, we have presented the main structural properties of various classes of MREs produced with and without a magnetic field. We have shown that the fillers together with the matrix in which they are embedded form usually hierarchically (two-level) fractal structures. We have presented the corresponding theoretical models and have obtained the main parameters from scattering data, namely, the fractal dimensions and the overall sizes of each structural level.

For a recently obtained MRE based on cotton fabric reinforced with a solution containing silicone rubber, carbonyl iron microparticles, silicone oil, and graphene nanoparticles as fillers

with various volume concentrations, we have shown in detail the fabrication process of a new class of smart membranes. The electrical and rheological properties of the membranes are greatly influenced by the quantity of fillers. In addition, they can be continuously modified in a magnetic field superimposed on an electrical field. We have shown that the components of the complex relative dielectric permittivity, the electrical conductivity, and the viscosity of the membranes are the result of complex interparticle interaction of the fillers inside the fractal polymer matrix. When the fillers themselves form fractal aggregates, this usually leads to formation of complex two-level hierarchical structures.

We have explained the electrical and rheological properties in the framework of dipolar approximation, where we have proposed a model based on the assumption that carbonyl iron microparticles become magnetic dipoles which attract each other. We have shown that the suggested theoretical model can describe with good accuracy the physical processes leading to the observed effects.

Acknowledgements

We are grateful to our partners from JINR-Dubna, UMF-Craiova, and UVT-Timisoara for the fruitful collaboration.

A. Appendix

In the following, we explain in more detail some important terms used throughout the chapter.

Small-angle scattering (SAS; neutrons, X-rays, light) is an experimental technique for investigating the structural properties of matter up to about 1 μm. This technique yields the elastic cross section per unit solid angle as a function of the momentum transfer (q) and describes, through a Fourier transform, the spatial density-density correlations of the system.

Radius of gyration (R_g) is the square root of the average density weighted squared distance of the scatterers from the center of the object and it is a measure of its overall size. In a SAS experiment, R_g is determined from the end of plateau at low q (Guinier region) on a double logarithmic scale.

erf is the error function (known also as Gauss error function) defined as

$$f(x) = \frac{1}{\sqrt{\pi}} \int_{-x}^{x} e^{-t^2} \mathrm{d}t$$

Fractal dimension (known also as Hausdorff dimension) is a measure of the degree of ramification (for mass fractals) or of the roughness of a surface (for surface fractals). Mathematically, it is defined by considering first a subset A of an n-dimensional Euclidean space, and $\{V)i\}$ the covering of A, with $a_i = \mathrm{diam}(V_i) \leq a$. Then, the α-dimensional Hausdorff measure of A is

$$m^{\alpha}(A) \equiv \lim_{a \to 0} \inf_{\{V_i\}} \sum_i a_i^{\alpha}, \quad \alpha > 0,$$

where the infimum is on all possible coverings. The fractal dimension D of the set A is defined by

$$D \equiv \inf\{\alpha : m^{\alpha}(A) = 0\} = \sup\{\alpha : m^{\alpha}(A) = +\infty\},$$

and it gives the value of α for which the Hausdorff measure jumps from zero to infinity. When $\alpha = D$, the measure can take any value between zero and infinity. However, for practical applications, this equation is difficult to use, and one usually resorts to other methods, such as mass–radius relation. For example, in the case of a deterministic (exact self-similar) fractal of length L, whose first iteration consists of elements of size $\beta_s L$, we have $M(L) = kM(\beta_s L)$, where M is the "mass" (i.e., mass, volume, surface, etc.). Then, using the last equation we have $k\beta_s^D = 1$, from which the fractal dimension can be obtained. In a SAS experiment, D is given by the absolute value of the scattering exponent in the fractal region.

Author details

Eugen Mircea Anitas[1,2]*, Liviu Chirigiu[3] and Ioan Bica[4]

*Address all correspondence to: anitas@jinr.ru

1 Joint Institute for Nuclear Research, Dubna, Moscow Region, Russian Federation

2 Horia Hulubei National Institute of Physics and Nuclear Engineering, Bucharest-Magurele, Romania

3 University of Medicine and Pharmacy, Craiova, Romania

4 West University of Timisoara, Timisoara, Romania

References

[1] Rabinow J. The magnetic fluid clutch. AIEE Trans. 1948;**67**:1308-1315. DOI: 10.1109/EE.1948.6444497

[2] Bica I, Liu YD, Choi HJ. Physical characteristics of magnetorheological suspensions and their applications. Journal of Industrial and Engineering Chemistry. 2013;**19**:394-406. DOI: 10.1016/j.jiec.2012.10.008

[3] Bica I, Balasoiu M, Bunoiu M, Iordaconiu L. Microparticles and electrodonductive magnetorheological suspensions. Romanian Journal of Physics. 2016;**61**:926-945

[4] Bunoiu M, Bica I. Magnetorheological elastomer based on silicone rubber, carbonyl iron and Rochelle salt: Effects of alternating electric and static magnetic fields intensities.

Journal of Industrial and Engineering Chemistry. 2016;**37**:312-318. DOI: 10.1016/j.jiec.2016.03.047

[5] Ginder JM, Nichols ME, Elie LD, Tardiff JL. Magnetorheological elastomers: Properties and applications. Proc. SPIE 3675, Smart Structures and Materials 1999. Smart Materials technologies. 1999. DOI: 10.1117/12.352787

[6] Bica I, Anitas EM. Magnetic field intensity and graphene concentration effects on electrical and rheological properties of MREs-based membranes. Smart Materials and Structures. 2017;**26**:105038(1-11). DOI: 10.1088/1361-665X/aa8884

[7] Deng HX, Gong XL. Application of magnetorheological elastomer to vibration absorber. Communications in Nonlinear Science and Numerical Simulation. 2008;**13**:1938-1947. DOI: 10.1016/j.cnsns.2007.03.024

[8] Shen Y, Golnarghi MF, Heppler GR. Experimental research and modeling of magnetorheological elastomers. Journal of Intelligent Materials Systems and Structures. 2004;**15**:2735. DOI: 10.1177/1045389X04039264

[9] Ginder JM, Schlotter WF, Nichols ME. Magnetorheological elastomers in tunable vibration absorbers. Proc. SPIE 4331, Smart Structures and Materials: Damping and Isolation. 2001;**4331**:103110. DOI: 10.1117/12.432694

[10] Watson JR, Canton M. Method and apparatus for varying the stiffness of a suspension bushing 1997. US Patent 5,609,353

[11] Bica I. Influence of the transverse magnetic field intensity upon the electric resistance of the magnetorheological elastomer containing graphite microparticles. Materials Letters. 2009;**63**:2230-2232. DOI: 10.1016/j.matlet.2009.07.032

[12] Bica I. Influence of magnetic field upon the electric capacity of a flat capacitor having magnetorheological elastomer as a dielectric. Journal of Industrial and Engineering Chemistry. 2009;**15**:605-609. DOI: 10.1016/j.jiec.2009.02.005

[13] Eem SH, Jung HJ, Koo JH. Application of MR elastomers for improving seismic protection of base-isolated structures. IEEE Transactions on Magnetics. 2011;**47**:2901-2904. DOI: 10.1109/TMAG.2011.2156771

[14] Liao GJ, Gong XL, Xuan SH, Kang CJ, Zong LH. Development of a real-time tunable stiffness and damping vibration isolator based on magnetorheological elastomer. Journal of Intelligent Materials Systems and Structures. 2012;**23**:25-33. DOI: 10.1177/1045389X11429853

[15] Chen L, Gong XL, Jiang WQ, Yao JJ, Deng XX, Li WH. Investigation on magnetorheological elastomers based on natural rubber. Journal of Materials Science. 2010;**42**:5483-5489. DOI: 10.1007/s10853-006-0975-x

[16] Bica I. Damper with magnetorheological suspension. Journal of Magnetism and Magnetic Materials. 2002;**241**:196-200. DOI: 10.1016/S0304-8853(02)00009-4

[17] Bica I, Anitas EM, Averis LME. Tensions and deformations in composites based on polyurethane elastomer and magnetorheological suspension: Effects of the magnetic

field. Journal of Industrial and Engineering Chemistry. 2015;**28**:86-90. DOI: 10.1016/j.jiec.2015.02.003

[18] Borin D, Gunther D, Hintze C, Heinrich G, Odenbach S. The level of cross-linking and the structure of anisotropic magnetorheological elastomers. Journal of Magnetism and Magnetic Materials. 2012;**324**:3452-3454. DOI: 10.1016/j.jmmm.2012.02.063

[19] Guinier A, Fournet G. Small-Angle Scattering of X-rays. New York: John Wiley & Sons; 1955. p. 263

[20] Brumberger H, editor. Modern Aspects of Small-Angle Scattering. New York: NATO ASI Series; 1995. p. 463

[21] Feigin LA, Svergun DI. Structure Analysis by Small-Angle X-ray and Neutron Scattering. New York and London: Plenum Press; 1987. p. 335

[22] Balasoiu M, Craus ML, Kuklin AI, Plestil J, Haramus V, Islamov AH, Erhan R, Anitas EM, Lozovan M, Tripadus V, Petrescu C, Savu D, Savu S, Bica I: Microstructure of magnetite doped elastomers investigated by SAXS and SANS. Journal of Optoelectronics and Advanced Materials 2008;**10**(11):2932-2935

[23] Balasoiu M, Anitas EM, Bica I, Erhan R, Osipov VA, Orelovich OL, Savu D, Savu S, Kuklin AI. SANS of interacting magnetic micro-sized Fe particles in a Stomaflex creme polymer matrix. Optoelectronics and Advanced Materials – Rapid Communications. 2008;**2**(11):730-734

[24] Anitas EM, Balasoiu M, Bica I, Osipov VA, Kuklin AI: Small-angle neutron scattering analysis of the microstructure of Stomaflex Creme - Ferrofluid based elastomers. Optoelectronics and Advanced Materials – Rapid Communications 2009;**3**(6):621-624

[25] Craus ML, Islamov AK, Anitas EM, Cornei N, Luca D: Microstructural, magnetic and transport properties of La0.5Pr0.2Pb0.3-xSrxMnO3 manganites. Journal of Alloys and Compounds 2014;**592**:121-126. DOI: 10.1016/j.jallcom.2014.01.002

[26] Balasoiu M, Craus ML, Anitas EM, Bica I, Plestil J, Kuklin AI: Microstructure of stomaflex based magnetic elastomers. Physics of the Solid State 2010;**52**(5):917-921. DOI: 10.1134/S1063783410050070

[27] Anitas EM, Bica I, Erhan RV, Bunoiu M, Kuklin AI. Structural properties of composite elastomeric membranes using small-angle neutron scattering. Romanian Journal of Physics. 2015;**60**(5-6):653-657

[28] Martin JE, Hurd AJ. Scattering from fractals. Journal of Applied Crystallography. 1987;**20**:61-78. DOI: 10.1107/S0021889887087107

[29] Schmidt PW. Small-angle scattering studies of disordered, porous and fractal systems. Journal of Applied Crystallography. 1991;**24**:414-435. DOI: 10.1107/S0021889891003400

[30] Bale HD, Schmidt PW. Small-angle X-ray-scattering investigation of submicroscopic porosity with fractal properties. Physical Review Letters. 1984;**53**:596-599. DOI: 10.1103/PhysRevLett.53.596

[31] Teixeira J. Small-angle scattering by fractal systems. Journal of Applied Crystallography. 1988;**21**(6):781-785. DOI: 10.1107/S0021889888000263

[32] Bica I, Anitas EM, Bunoiu M, Vatzulik B, Juganaru I. Hybrid magnetorheological elastomer: Influence of magnetic field and compression pressure on its electrical conductivity. Journal of Industrial and Engineering Chemistry. 2014;**20**:3994-3999. DOI: 10.1016/j.jiec.2013.12.102

[33] Bica I, Anitas EM, Averis LME, Bunoiu M. Magnetodielectric effects in composite materials based on paraffin, carbonyl iron and graphene. Journal of Industrial and Engineering Chemistry. 2015;**21**:1323-1327. DOI: 10.1016/j.jiec.2014.05.048

[34] Bica I, Anitas EM, Chirigiu L, Bunoiu M, Juganaru I, Tatu RF: Magnetodielectric effects in hybrid magnetorheological suspensions. Journal of Industrial and Engineering Chemistry 2015;**22**:53-62. DOI: 10.1016/j.jiec.2014.06.024

[35] Bica I, Anitas EM, Averis LME. Influence of magnetic field on dispersion and dissipation of electric field of low and medium frequencies in hybrid magnetorheological suspensions. Journal of Industrial and Engineering Chemistry. 2015;**27**:334-340. DOI: 10.1016/j.jiec.2014.09.047

[36] Bica I, Anitas EM, Chirigiu L. Magnetic field intensity effect on plane capacitors based on hybrid magnetorheological elastomers with graphene nanoparticles. Journal of Industrial and Engineering Chemistry. 2017;**56**:407-412. DOI: 10.1016/j.jiec.2017.07.039

[37] Brumberger H, editor. Modern Aspects of Small-Angle Scattering. New York: NATO ASI Series; 1995. p. 463

[38] Feigin LA, Svergun DI. Structure Analysis by Small-Angle X-ray and Neutron Scattering. New York and London: Plenum Press; 1987. p. 335

[39] Beaucage G. Approximations leading to a unified exponential/power-law approach to small-angle scattering. Journal of Applied Crystallography. 1995;**28**:717-728. DOI: 10.1107/S0021889895005292

[40] Anitas EM. Small-angle scattering from fat fractals. European Physical Journal B. 2014;**87**:139. DOI: 10.1140/epjb/e2014-41,066-9

[41] Cherny AY, Anitas EM, Osipov VA, Kuklin AI. Small-angle scattering from multiphase fractals. Journal of Applied Crystallography. 2014;**47**:198-206. DOI: 10.1107/S1600576713029956

[42] Anitas EM. Microscale fragmentation and small-angle scattering from mass fractals. Advances in Condensed Matter Physics. 2015;**2015**, ID 501281. DOI: 10.1155/2015/501281

[43] Anitas EM. A structural model for scattering intensities with multiple fractal regions of variable length. Journal of Optoelectronics and Advanced Materials. 2015;**17**:1122-1127

[44] Anitas EM. Scattering structure factor from fat fractals. Romanian Journal of Physics. 2015;**60**:647-652

[45] Cherny AY, Anitas EM, Osipov VA, Kuklin AI. The structure of deterministic mass, surface and multi-phase fractals from small-angle scattering data. Romanian Journal of Physics. 2015;**60**:658-663

[46] Anitas EM, Osipov VA, Kuklin AI, Cherny AY. Influence of randomness on small-angle scattering from deterministic mass fractals. Romanian Journal of Physics. 2015;**61**:457-463

[47] Anitas EM, Slyamov A, Todoran R, Szakacs Z. Small-angle scattering from nanoscale fat fractals. Nanoscale Research Letters. 2017;**12**:389. DOI: 10.1186/s11671-017-2147-0

[48] Anitas EM, Slyamov A. Structural characterization of chaos game fractals using small-angle scattering analysis. PLOS One. 2017;**12**(7):e0181385. DOI: 10.1371/journal.pone.0181385

[49] Melle S. Study of the Dynamics in Magnetorheological Suspensions Subject to External Fields by Means of Optical Techniques. Madrid: University of Madrid; 1995. PhD Thesis

[50] Jones TB. Electromechanics of Particles. New York, USA: Cambridge University Press; 1995

[51] Liu J. Models of Electromagnetic Properties of Composite Media. Iowa, USA: Iowa State University; 2012. http://lib.dr.iastate.edu/etd/12695. PhD Thesis

IntechOpen

IntechOpen

IntechOpen